Morphological and Kinetic Studies on Hexagonal Tungstates

Alexej Michailovski,[†] Ragnar Kiebach,[‡] Wolfgang Bensch,[‡] Jan-Dierk Grunwaldt,[§] Alfons Baiker,[§] Sridhar Komarneni,[||] and Greta R. Patzke*,[†]

Laboratory of Inorganic Chemistry, ETH Zurich, CH-8093 Zurich, Switzerland, Institute of Inorganic Chemistry, University of Kiel, Olshausenstrasse 40, D-24098 Kiel, Germany, Institute for Chemical and Bioengineering, ETH Zurich, CH-8093 Zurich, Switzerland, and 205 Materials Research Laboratory, The Pennsylvania State University, University Park, Pennsylvania 16802

Received May 3, 2006. Revised Manuscript Received October 26, 2006

Formation of nanostructured hexagonal alkali tungstates (HTBs) from ammonium metatungstate (AMT) and alkali chlorides has been investigated by a combined strategy encompassing in situ spectroscopic techniques and hydrothermal synthetic studies. They demonstrate how the morphology of the HTBs can be tuned by the straightforward hydrothermal reaction of ammonium metatungstate with the choice of appropriate alkali chlorides. The resulting particle shapes vary from highly anisotropic fibers to multilevel assemblies of hierarchically grown nanorods. Microwave-hydrothermal techniques have further expanded this morphological spectrum. Next, the growth process of alkali HTBs was explored for selected cases by combination of in situ EXAFS and EDXRD investigations. They both show that nucleation starts after a certain induction time and is strongly dependent on the concentration. Though the individual kinetics of alkali HTB formation differ slightly from each other, all alkali cations have a nucleation-controlled growth mechanism in common.

1. Introduction

Tungsten bronzes (M_xWO_3) and tungstates ($M_xWO_{3+x/2}$) with open structures readily incorporate cations, such as hydrogen or lithium, so that modification of the host tungstate framework opens up new options for synthesizing tailor-made materials.[1] As a consequence, they have attracted considerable interest due to their unique chemical, electrochemical, and electronic properties.[2] Hence, they are promising materials for applications as active electrodes, e.g., in electrochromic devices, large-scale static displays,[3] and catalysis.[4] Transformation of these important tungstate-based materials into nanomaterials with anisotropic morphologies is just about to be explored.[5] Recent results on formation of hexagonal WO_3 nanosheets from $BaWO_4$−polymer nanohybrids revealed the general relevance of such morphological investigations for the controlled production of functional metal oxides.[6] Furthermore, morphology-synthesis studies on tungstic acid precipitates have unraveled that the delicate relationships between the preparative parameters and the resulting particle shape require profound parameter studies.[7]

Three main types of $M_xWO_3/M_xWO_{3+x/2}$ (M = H, NH_4, Li−Cs) tungstate frameworks have been described: the cubic form, the hexagonal tungstates (HTB), and the pyrochlore (P) type.[3] The majority of the $M_xWO_{3+x/2}$ tungstates adopt either the HTB or the P form. Both structure types contain tunnels: in the HTB phase, the one-dimensional tunnels run along the *c* axis, whereas they intersect in a three-dimensional fashion in the P type.[2,8] Consequently, the two phases exhibit different intercalation behavior and reactivity: the P type preferably hosts the larger cations (Rb, Cs),[9,10] readily intercalates lithium cations, and exhibits an active redox chemistry.[11] 2D-variation of the P-type has been reported for $xMO{\cdot}WO_3$ (M = Tl, Ba, Pb) systems.[12] The HTB $M_xWO_{3+x/2}$ tungstates are less prone to ion-exchange processes but more suitable for lithium intercalation.[11] Their redox chemistry ($M_xWO_3 \leftrightarrow M_xWO_{3+x/2}$) involves diffusion of oxygen atoms in and out of the hexagonal channel systems so that they must move around the incorporated alkali cations.[13] The latter can be located in either the hexagonal cavity or the preceding window site of the hexagonal tunnel. Depending on the size and amount of incorporated cations,

* To whom correspondence should be addressed. Phone: +41 44 632 6743. Fax: +41 44 632 1149. E-mail: patzke@inorg.chem.ethz.ch.
[†] Laboratory of Inorganic Chemistry.
[‡] University of Kiel.
[§] Institute for Chemical and Bioengineering.
[||] Pennsylvania State University.

(1) Yu, A.; Kumagai, N.; Liu, Z.; Lee, Y. *J. Solid State Electrochem.* **1998**, *2*, 394.
(2) Guo, J.-D.; Reis, K. P.; Whittingham, M. S. *Solid State Ionics* **1992**, *305*, 53−56.
(3) Whittingham, M. S. In *Solid State Devices*; Chowdari, B. V. R., Radhakrishnan, S., Eds.; World Scientific: Singapore, 1988.
(4) Francke, L.; Durand, E.; Demourgues, A.; Vimont, A.; Daturi, M.; Tressaud, A. *J. Mater. Chem.* **2003**, *13*, 2330.
(5) Cao, G.; Song, X.; Yu, H.; Fan, C.; Yin, Z.; Sun, S. *Mater. Res. Bull.* **2006**, *41*, 232.
(6) Oaki, Y.; Imai, H. *Adv. Mater.* **2006**, *18*, 1807.
(7) Balázsi, Cs.; Pfeifer, J. *Solid State Ionics* **1999**, *124*, 73.
(8) Guo, J.-D.; Whittingham, M. S. *Int. J. Modern Phys. B* **1993**, 4145.
(9) Chévrier, G.; Tuoboul, M.; Driouiche, A.; Figlarz, M. *J. Mater. Chem.* **1992**, *2* (6), 639.
(10) Driouiche, A.; Abraham, F.; Touboul, M.; Figlarz, M. *Mater. Res. Bull.* **1991**, *26*, 901.
(11) Reis, K. P.; Ramanan, A.; Whittingham, M. S. *J. Solid State Chem.* **1992**, *96*, 31.
(12) Kudo, T.; Oi, J.; Kishimoto, A.; Hiratani, M. *Mater. Res. Bull.* **1991**, *26*, 779.
(13) Reis, K. P.; Prince, E.; Whittingham, M. S. *Chem. Mater.* **1992**, *4*, 307.

10.1021/cm061020o CCC: $37.00
Published on Web 12/20/2006

two different structural models have been proposed. Sodium cations are too small to stabilize the HTB framework at higher temperatures, and they are situated in the hexagonal channel windows of HTB−$Na_xWO_{3+x/2}$·nH_2O where they are "sandwiched" by H_2O molecules (or hydroxyl ions).[13,14] Larger cations (M = K−Cs) can only be incorporated into the hexagonal tunnels of HTB−xM_2O·WO_3 on two suitable sets of positions so that the maximum extent of cation incorporation should be limited to $x \leq 2/9$.[12] However, higher contents are often analytically determined, and they are explained in terms of a tungsten vacancy model ($M_xW_{1-y/6}O_3$, with $y = 6x/(6 + x)$).[12,15,16]

Whereas HTB and P alkali tungstates have preferably been accessed through soft chemistry routes (Table S1), considerably less is known about their availability as nanoscale materials.[17,18] A summary goes beyond the scope of this paper but is given in the Supporting Information (Table S1).

In order to address a specific structure type, careful adjustment of the cation size, the synthetic parameters (especially the pH value[11]), and the precursor material is required (Table S1). The resulting structure type strongly depends upon the tungstate species present in solution. Their kinetic study is demanding because the reactions involved differ widely with respect to their rates.[2] Therefore, preparation of nanoscale HTB/P tungstates is a challenging task.[19] However, the preparative effort is worthwhile because hexagonal tungstates offer some specific facilities that might be enhanced through nanosctructured morphologies, as recently observed for other classes of tungstates, e.g., luminescent MWO_4 materials (M = Pb, Cd, Sr).[20] In a similar fashion, the outstanding ion-exchange properties of HTB phases in the removal of ^{137}Cs and ^{90}Sr from radioactive waste[21] could further benefit from nanoscale particles shapes. The same goes for the catalytic properties and potential use as electrode materials that arise from the proton and electronic conductivity of ammonium HTBs.[17] Moreover, the specific capacities and Li^+ cycling behavior of Li−HTBs are often superior to other tungstates, and this effect is likely to be enhanced through control of the particle size and shape.[1] Thus, we present a convenient hydrothermal pathway to access anisotropic and nanostructured hexagonal tungstates in the following study.

Starting from our previous work on the synthesis of nanostructured ammonium pyrochlore tungstates from ammonium metatungstate (AMT, $(NH_4)_6[H_2W_{12}O_{40}]$·$2H_2O$),[22] we systematically studied the hydrothermal formation of nanostructured alkali tungstates in MCl/AMT systems (M = Li−Cs) with respect to morphochemistry and kinetics. To the best of our knowledge, a comprehensive morphological study of the alkali tungstates has never been undertaken. Recently, microwave-hydrothermal methods have emerged as a powerful preparative method to access oxidic nanoparticles.[23] Since little is known about alkali tungstate formation upon microwave irradiation,[24] selected MCl/AMT systems were additionally investigated under microwave-hydrothermal conditions.[25] Finally, we evaluated the kinetics of nanostructured alkali tungstate formation using both in situ EXAFS and EDXRD methods.[26] As little is known about the hydrothermal formation mechanisms of Mo/W-oxide materials, we hereby present the second part of a comprehensive morphological and kinetic work: in the first study, use of complementary in situ EXAFS and EDXRD techniques is demonstrated for monitoring of MoO_3 rod formation,[26] while in the following second study, the according kinetic information on hexagonal tungstates is provided. The third part is focused on the kinetics of mixed (Mo/W)-nanoscale oxide synthesis.[27] The latter exhibit properties in ion exchange,[8] sensor technology,[28] and catalysis[29] that are superior to their binary counterparts. For the controlled hydrothermal preparation of such high-performance ternary materials, deeper insight into the reaction mechanisms of nanostructured tungsten oxides is indispensable.

2. Experimental Procedures

2.1. Standard Hydrothermal Conditions. The following standard hydrothermal procedure was applied for the preparation of alkali/ammonium tungstates from ammonium metatungstate (AMT, cf. above): 248 mg of AMT (1 mmol of W), 2 mL of 25 vol. % acetic acid (HAc), and 2 mmol of MCl (M = Li−Cs) were added to a Teflon-lined stainless-steel autoclave with a capacity of 23 mL. The autoclave was then sealed, heated for 2 days at 180 °C, and subsequently cooled to room temperature. The resulting precipitate was collected by filtration, washed with distilled H_2O, EtOH, and Et_2O or acetone, and dried in air.

2.2. Microwave-Hydrothermal Experiments. The microwave-hydrothermal (M-H) experiments were performed using a MARS5 (CEM Corp., Matthews, NC) microwave digestion system. The microwave system operates at a frequency of 2.45 GHz with a maximum power of 1200 W. The experiments were carried out in double-walled digestion vessels having an inner nonreactive

(14) Reis, K. P.; Ramanan, A.; Whittingham, M. S. *Chem. Mater.* **1990**, *2*, 219.
(15) Oi, J.; Kishimoto, A.; Kudo, T. *J. Solid State Chem.* **1993**, *103*, 176.
(16) Tsuyumoto, I.; Kishimoto, A.; Kudo, T. *Solid State Ionics* **1993**, *59*, 211.
(17) (a) Huo, L.; Zhao, H.; Mauvy, F.; Fourcade, S.; Labrugere, C.; Pouchard, M.; Grenier, J.-C. *Solid State Sci.* **2004**, *6*, 679. (b) Coucou, A.; Figlarz, M. *Solid State Ionics* **1988**, *1762*, 28−30. (c) Feldmann, C.; Jungk, H.-O. *Angew. Chem., Int. Ed.* **2001**, *40*, 359.
(18) (a) Kumagai, N.; Matsuura, Y.; Umetzu, Y.; Tanno, K. *Solid State Ionics* **1992**, 324, 53−56. (b) Laruelle, S.; Figlarz, M. *J. Solid State Chem.* **1994**, *111*, 172. (c) Reis, K. P.; Ramanan, A.; Whittingham, M. S. *J. Solid State Chem.* **1991**, *91*, 394.
(19) Polleux, J.; Pinna, N.; Antonietti, M.; Niederberger, M. *J. Am. Chem. Soc.* **2005**, *127*, 15595.
(20) Ryu, J. H.; Koo, S.-M.; Chang, D. S.; Yoon, J.-W.; Lim, C. S.; Shim, K. B. *Electrochem. Solid State Lett.* **2005**, *8*, D15.
(21) Griffith, C. S.; Luca, V. *Chem. Mater.* **2004**, *16*, 4992.
(22) Michailovski, A.; Krumeich, F.; Patzke, G. R. *Mater. Res. Bull.* **2004**, *39*, 887.
(23) (a) Katsuki, H.; Shiraishi, A.; Komarneni, S.; Moon, W. J.; Toh, S.; Kaneko, K. *J. Ceram. Soc. Jpn.* **2004**, *112*, 384. (b) Komarneni, S.; D'Arrigo, M. C.; Leonelli, C. G.; Pellacani, C.; Katsuki, H. *J. Am. Ceram. Soc.* **1998**, *81*, 3041.
(24) Pfeifer, J.; Badaljan, E.; Tekula-Buxbaum, P.; Kovács, T.; Geszti, O.; Tóth, A. L.; Lunk, H.-J. *J. Cryst. Growth* **1996**, *169*, 727.
(25) (a) Komarneni, S. *Curr. Sci.* **2003**, *85*, 1730. (b) Lu, Q. Y.; Gao, F.; Komarneni, S. *J. Mater. Res.* **2004**, *19*, 1649.
(26) Michailovski, A.; Grunwaldt, J.-D.; Baiker, A.; Kiebach, R.; Bensch, W.; Patzke, G. R. *Angew. Chem., Int. Ed.* **2005**, *44*, 5643.
(27) (a) Michailovski, A.; Krumeich, F.; Patzke, G. R. *Chem. Mater.* **2004**, *16*, 1126. (b) Michailovski, A.; Kiebach, R.; Grunwaldt, J.-D.; Baiker, A.; Bensch, W.; Patzke, G. R. Manuscript in preparation.
(28) Merdrignac-Conanec, O.; Moseley, P. T. *J. Mater. Chem.* **2002**, *12*, 1779.
(29) Ivanov, K.; Mitov, I.; Krustev, S. *J. Alloys Compd.* **2000**, *309*, 57.

Teflon PFA liner and an outer Ultem polyetherimide shell of high mechanical strength. Temperature and pressure probes allow the reaction to be controlled by monitoring the temperature and pressure within a control vessel. The maximum operating temperature and pressure for the system are 240 °C and 350 psi, respectively. In a typical procedure, 248 mg of AMT (1 mmol of W, 5 mL of 25 vol. % acetic acid (HAc) and 1 or 5 mmol of MCl (M = Li−Cs)) was treated for 4 h at 180 °C using the above microwave digestion system.

2.3. Analytical Methods. X-ray powder diffraction analyses were conducted on a STOE STADI-P2 diffractometer in transmission mode (flat sample holders, Ge-monochromated Cu $K\alpha_1$ radiation) equipped with a position-sensitive detector (resolution ca. 0.01° in 2θ).

For scanning electron microscopy (SEM), performed on a LEO 1530 (FEG) microscope with 1 keV electrons, samples were dispersed in ethanol and subsequently deposited on a silicon wafer. A CamScan CS-44 electron microscope with an EDAX-Phoenix energy-dispersive X-ray spectrometer (EDXS) was employed for approximate elemental analyses. The scanning transmission electron microscopy (STEM) image was recorded on a Philips Tecnai 30F microscope, operated at 300 kV (field emission cathode). In the STEM mode, the electron beam was placed on a selected spot, and elemental analysis by energy-dispersive X-ray spectroscopy (EDS, EDAX detector) was performed there.

FTIR spectra were recorded on a Perkin-Elmer Spectrum 2000 FTIR spectrometer in the range from 500 to 4000 cm^{-1}. C, H, and N analysis was carried out by means of combustion test methods on a LECO CHN-900. Alkali contents were determined by laser ablation inductively coupled plasma mass spectroscopy (LA-ICP-MS). Laser ablation sampling was performed using an ArF 193 nm excimer laser (GeoLas Q, MicroLas, Göttingen, Germany) which was coupled to an ICP-MS instrument (Elan 6100 DRC+ Perkin-Elmer, SCIEX, Concord, Ontario, Canada).[30]

2.4. In Situ EXAFS Experiments. The in situ X-ray absorption spectroscopy experiments were performed at ANKA-XAS (Karlsruhe, Germany) using an EXAFS cell that allows monitoring both the bottom and the middle of the autoclave cell up to 200 bar and 200 °C.[31] The cell was equipped with a PEEK-inlet, and in the present experiment the penetration length was about 5 mm through the solution. A Si(111) double-crystal monochromator was used, and higher harmonics were effectively removed by detuning of the crystals to 70% of the maximum intensity. Three ionization chambers before and after the in situ cell and a reference foil for energy calibration were used for the incident and out coming X-ray intensities. The beam size was cut to 5 × 1 mm, and the in situ batch reactor cell was aligned using the x,z,θ table. EXAFS scans around the W L_3-edge were recorded between 10.05 and 11.8 keV under stationary conditions (liquid solution and solid material) and calibrated using the W reference foil (energy range 10.185−10.300 keV). Faster spectra during the change of the reaction conditions were recorded around the W L_3-edge. Note that the solid material crystallizes at the wall so that both the solid and the liquid are measured at the same time. The raw data were background corrected, normalized, and Fourier transformed using the WINXAS 3.0 software.[32] The experiment was performed in the following way: The spectroscopic cell was filled with 3 mL of a solution of AMT in 25 vol. % HAc (0.05 M in W), closed, and heated to 200 °C stepwise. Then the hydrothermal reaction was performed over a time period of 4 h at 200 °C and cooled down, and the material was analyzed by EXAFS, XRD, and SEM. A second experiment was analogously performed adding CsCl (0.1 mol/L).

2.5. In Situ EDXRD Experiments. The in situ energy-dispersive X-ray diffraction experiments were performed at HASYLAB Beamline F3 that received white synchrotron radiation from a bending magnet with a critical energy of 16 keV (DORIS ring with positron beam energy of 4.5 GeV). An energy range from 13.5 to 65 keV can be observed with a maximum at about 20 keV. The diffracted beam is monitored by a nitrogen-cooled solid-state germanium detector. The detector angle was chosen so that all important Bragg reflections can be detected. The *d*-spacing range is given by $E = 6.199/(d \cdot \sin\theta)$. With a detector angle of approximately 1.90° the observable *d*-spacing range is 2.9−13.8 Å. The energy resolution $\Delta d/d$ is about 10^{-2} above 26 keV. The beam was collimated to 0.2 mm, giving the best results. A more detailed experimental description can be found in the literature.[33,34] For the in situ investigations autoclaves with glass liners with an internal diameter of 10 mm and a volume of 10 mL were used. They were filled with 1.5 mL of a solution of AMT in 25 vol. % HAc (0.67 M in W) and 1.5 mmol of MCl (M = Li−Cs), closed, and heated to 200 °C.

3. Experimental Results

3.1. Hydrothermal Synthesis. As outlined in the introduction, the alkali tungstate type emerging from a given hydrothermal reaction is a function of the cation radius and the synthetic conditions. In the MCl/AMT/HAc (M = Li−Cs) systems, the ammonium cations of the AMT precursor may be incorporated into the newly formed hexagonal tunnels in addition to the alkali cations. Extensive optimization experiments aiming for phase pure nanoparticles exhibiting uniform morphologies with large aspect ratios (if applicable) were conducted starting from a standard hydrothermal procedure (cf. Experimental Procedures). For hydrothermal experiments conducted in acetic acid solutions, the initial and final pH values are in the range of 2−3. When H_2O is used instead of acetic acid, the initial pH is between 5 and 6. Room-temperature precipitation experiments in the CsCl/AMT/HAc and CsCl/AMT/H_2O systems led to formation of the Keggin cluster compound $Cs_6[H_2W_{12}O_{40}]\cdot 2H_2O$. Its crystal structure is one of the rare examples of a homonuclear alkali Keggin compound.[35] The presence of $Cs_6[H_2W_{12}O_{40}]\cdot 2H_2O$ indicates that the Keggin cluster anion, $[H_2W_{12}O_{40}]^{6-}$, is the predominant species in solution.

A number of hydrothermal parameters have been systematically varied, and it turns out that the particle shape can be most conveniently addressed by adjusting the concentration of the precursor material. Furthermore, variations in pH and reaction time affect the particle morphology.

Therefore, the kinetics of the transformation of AMT into HTB tungstates has been investigated with the help of ex situ and in situ experiments (cf. below).

3.1.1. Role of the Alkali Cations: Structural and Analytical Chemistry. Table 1 provides a summary of the hydrothermal

(30) (a) Günther, D.; Hattendorf, B. *Trends Anal. Chem.* **2005**, *24*, 255. (b) Ottinger, F.; Kroslakova, I.; Hametner, K.; Reusser, E.; Nesper, R.; Günther, D. *Anal. Bioanal. Chem.* **2005**, *383*, 489.
(31) Grunwaldt, J.-D.; Ramin, M.; Rohr, M.; Michailovski, A.; Patzke, G. R.; Baiker, A. *Rev. Sci. Instrum.* **2005**, *76*, 054104.
(32) Ressler, T. *J. Synchrotron Radiat.* **1998**, *5*, 118.
(33) Engelke, L.; Schäfer, M.; Porsch, F.; Bensch, W. *Eur. J. Inorg. Chem.* **2003**, *3*, 506.
(34) Engelke, L.; Schäfer, M.; Schur, M.; Bensch, W. *Chem. Mater.* **2001**, *13*, 1383.
(35) Michailovski, A.; Patzke, G. R. Manuscript in preparation.

Table 1. Synthetic Profiles of the Alkali Cations in the Hydrothermal Formation of Alkali Tungstates(VI)

cation	phase	typical morphology	representative composition (HTB)
Li^+	HTB/O	HTB: rods (*d* 20−30 nm, *l* 200−400 nm) O: μm-sized flower-like aggregates with dendritic nanorods	$(NH_4)_{0.15}Li_{0.14}W_{0.95}O_3{\cdot}0.85H_2O$
Na^+	HTB	rods: μm-scale lengths (max. 12 μm), *d* ca. 100 nm	$(NH_4)_{0.12}Na_{0.20}W_{0.95}O_3{\cdot}0.61H_2O$
K^+	HTB	rods: μm-scale lengths (max. 3 μm), *d* ca. 100 nm	$(NH_4)_{0.02}K_{0.33}W_{0.94}O_3{\cdot}0.45H_2O$
Rb^+	HTB/P	HTB: stacked rods (ca. 200 × 800 nm), hierarchical patterns	$Rb_{0.31}W_{0.95}O_3{\cdot}nH_2O$
Cs^+		P: cubic microcrystals	$Cs_{0.33}W_{0.95}O_3{\cdot}0.22H_2O$
NH_4^+(AMT-ref)	HTB	rods: *d* 7−15 nm, *l* 80−250 nm	$(NH_4)_{0.26}W_{0.96}O_3{\cdot}nH_2O$

parameter study in the MCl/AMT systems: the smallest cation Li^+ supports formation of orthorhombic (O) lithium tungstates only under special conditions (cf. section 3.1.2.1), and the HTB phase generally dominates in the MCl/AMT (M = Li−K) systems. Note that the crystallinity of the products considerably decreases in the presence of potassium cations, as observed in previous studies.[18a] Among the MCl/AMT (M = Rb, Cs) systems, the reaction conditions had to be optimized to obtain phase pure HTB or P alkali tungstates. As expected, the P-type tungstates are preferably formed in the presence of the larger Cs^+ cation.[9] The larger the cation, the more pronounced is its stabilizing influence upon the tungstate channel system: a competitive experiment involving the simultaneous reaction of AMT with equimolar amounts of the entire MCl series (M = Li−Cs) led to exclusive incorporation of Cs^+ into HTB−$Cs_{0.27}W_{0.96}O_3{\cdot}nH_2O$. The fraction of ammonium cations incorporated into the HTB alkali tungstates depends on the size of the alkali cation. According to elemental analyses, the Li− and Na−HTB systems readily incorporate ammonium cations whereas the potassium-containing compounds take up only a minimal fraction of NH_4^+. The Rb− and Cs−HTB phases are practically ammonium free. The water content of the samples follows the same trend and decreases from the Li− to the Cs−HTB tungstates. The results are in line with the IR spectra of the HTB alkali tungstates (Figure 1): the intensity of the NH_4^+ bending vibration around 1400 cm^{-1} decreases from the Li− to the Cs−HTB tungstate and so does the OH bending vibration around 1600 cm^{-1}.[18a] The narrow OH bending vibrations for Li− and Na−HTB indicate the presence of structural water molecules.

LA-ICP-MS techniques (cf. Experimental Procedures) were employed for determination of M:W (M = Li−Cs) ratios. The ranges for the individual cations are displayed in Figure 2.

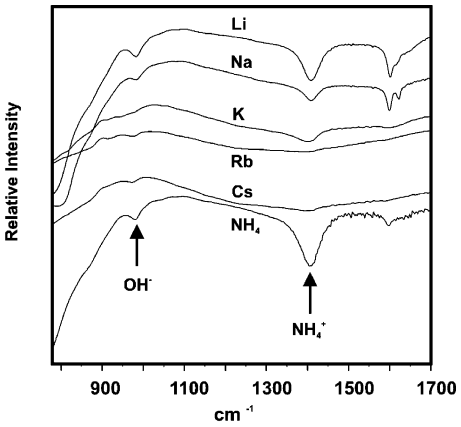

Figure 1. Representative IR spectra of HTB−alkali tungstates(VI) (arrow indicates the characteristic NH_4^+ and OH^- bending vibration around 1400 and 1600 cm^{-1}, respectively).

Li^+ and Na^+ can be substituted by NH_4^+ over a wide compositional range, and most of the alkali tungstates exceed the limiting M:W ratios of 0.17:1 (M = Na)[13] or 0.22:1 (M = K−Cs)[12] for incorporation of cations into the hexagonal tunnels (cf. representative compositions in Table 1). Therefore, they are described in terms of the above-mentioned tungsten vacancy model.[12]

3.1.2. Role of the Alkali Cations: Morphology. The alkali cations not only exert a structure-directing effect, but they also lead to characteristic nanostructured morphologies of the alkali tungstates (Table 1). Reference hydrothermal experiments in the AMT/HAc system afford HTB−$(NH_4)_{0.26}W_{0.96}O_3{\cdot}nH_2O$ nanorods (cf. Figure 8a), whereas the smaller cations (M = Li − K) lead to formation of fibrous HTB tungstates with microscale lengths and diameters around 100 nm. Maximum aspect ratios are obtained in the presence of sodium cations. The larger cations (M = Rb, Cs) yield nanostructured hexagonal phases consisting of small, stacked nanorods that tend to arrange into hierarchical patterns (Table 1).

In Table 2 the change in morphology induced by selected parameter variations is compared to the results obtained under standard conditions (cf. Experimental Procedures). Selected hydrothermal parameters were optimized to improve the morphological uniformity and the aspect ratio of the emerging hexagonal tungstate particles. Low initial AMT concentrations and replacement of acetic acid by H_2O exerted the most significant influence on the tungstate morphology.

3.1.2.1. LiCl/AMT System. Figure 3 illustrates how the aspect ratio of Li−HTB nanorods obtained under standard conditions can be enhanced in the presence of low (0.07 M) tungstate concentrations (Figure 3a).

Further dilution of the precursor material to 0.007 M (Figure 3b, c) leads to formation of orthorhombic lithium tungstate with a flower-like growth pattern that is characteristic of orthorhombic tungstates (cf. the morphology of orthorhombic ammonium tungstates, Figure 8b). The small

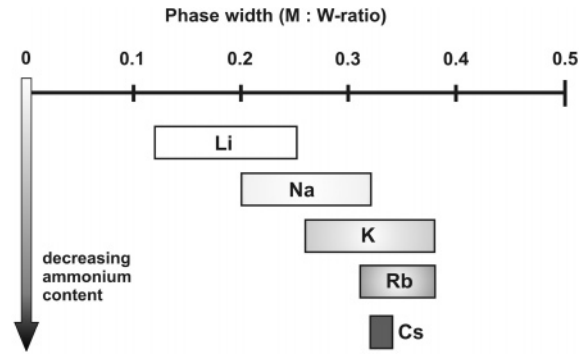

Figure 2. M:W ratio (M = Li−Cs) in HTB−alkali tungstates(VI) as determined from LA-ICP-MS techniques.

Table 2. Effects of Hydrothermal Parameter Variations on the Morphology of Nanostructured Alkali Tungstates(VI) (bold: Optimum Results; a.r. = Aspect Ratio)

parameter	uniformity/a.r. unchanged	uniformity/a.r. improved	uniformity/a.r. deteriorated
MCl:AMT = 0.25:1	Li, Na		K, Rb, Cs
MCl:AMT = 4:1	K, Cs (P)	Rb	Li, Na
MCl/AMT/H_2O	Na, Rb (P), Cs (P)	Li	K
c(W) = 0.07 M		**Li**, Na, K, Cs (P)	Rb
c(W) = 0.07 M, H_2O		Na, **K**, Rb (P)	Li, Cs (P)
c(W) = 0.007 M		Li (orth.), Na, K, **Cs**	Rb
c(W) = 0.007 M, H_2O		**Na, Rb**	Cs (P)

nanorods emerging from the surface of the micrometer-sized "flower leaves" might exhibit a hexagonal structure because the broadened reflections in the XRD patterns of nanostructured O and HTB tungstates differ only with respect to an additional reflection at $2\theta = 18°$ in the orthorhombic phase.[36]

3.1.2.2. NaCl/AMT System. Under standard hydrothermal conditions the morphology of Li− and Na−HTB tungstate nanorods is almost identical (cf. Figure 3a and Figure S2). However, low tungstate concentration affords Na−HTB tungstate rods in the NaCl/AMT/H_2O system with microscale lengths and diameters around 100 nm (Figure 4a). Their aspect ratio can be maximized when the tungstate concentration is decreased to 0.007 M (Figure 4a,b).

3.1.2.3. KCl/AMT System. Although the KCl/AMT/H_2O system provides well-developed nanorods with aspect ratios similar to those obtained from NaCl solutions (cf. Figures 4c and S2b), the XRD patterns of the products reveal that they are almost amorphous, and the yields are considerably lower than in the sodium-based systems. Tungsten concentrations lower than 0.07 M did not afford an increase in aspect ratio or crystallinity.

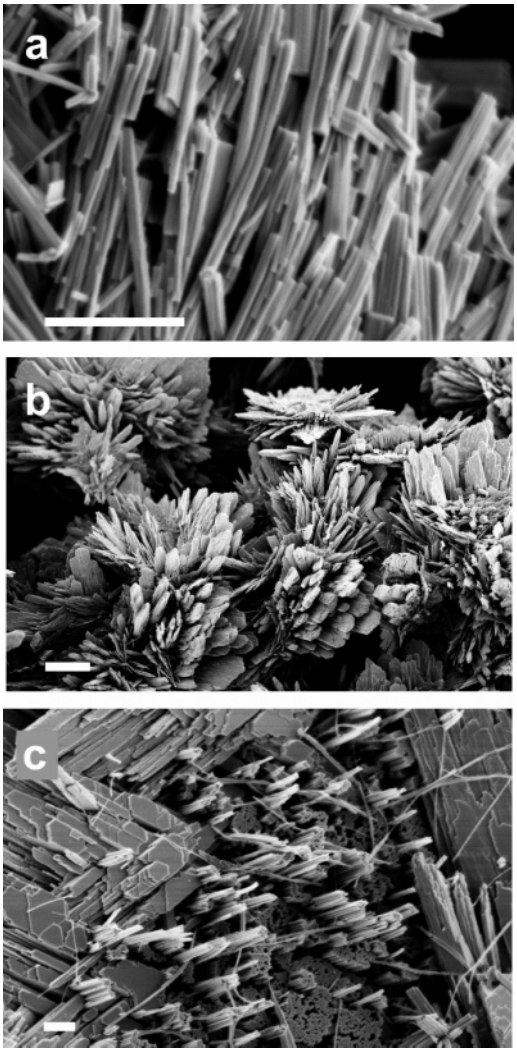

Figure 3. Representative SEM images of lithium tungstates synthesized (a) under standard conditions (scale bar = 300 nm) and (b, c) from highly diluted AMT solutions (c(W) = 0.007 M; scale bar = 3 μm and 300 nm, respectively).

3.1.2.4. RbCl/AMT Systems. The presence of the larger rubidium cations induces a significant morphological change: Rb−HTB tungstates are obtained as cylindrical stacks consisting of small nanorods (Figure 5a, Table 1). They tend to agglomerate under standard conditions (Figure 6b). Their intergrowth can be reduced by applying a low initial tungstate concentration (c(W) = 0.007 M) in H_2O (Figure 5c). Unlike in the Na- and K-based systems, the aspect ratio of the hierarchically grown nanorods remains unchanged upon precursor dilution.

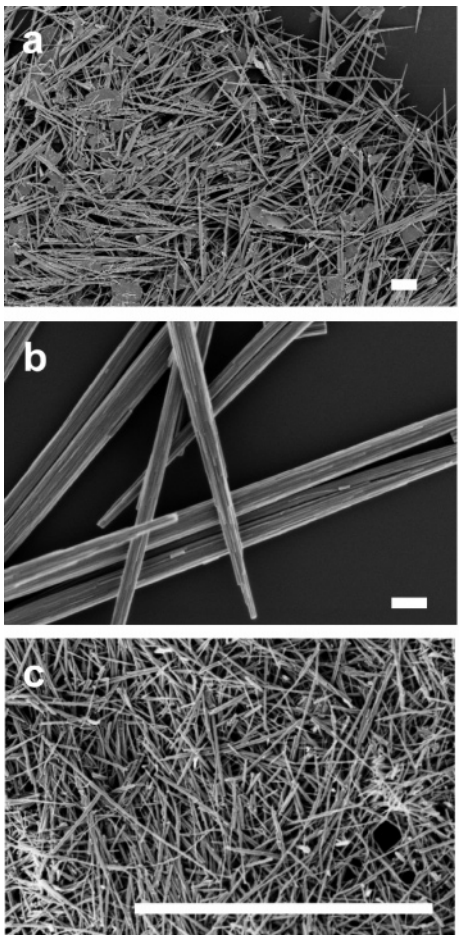

Figure 4. Representative SEM images of (a, b) Na−HTB tungstate rods synthesized from highly diluted AMT solutions (c(W) = 0.007 M in H_2O; scale bar = 3 μm and 300 nm, respectively) and (c) K−HTB tungstate rods (scale bar = 3 μm) synthesized in the KCl/AMT/H_2O system with standard precursor concentration.

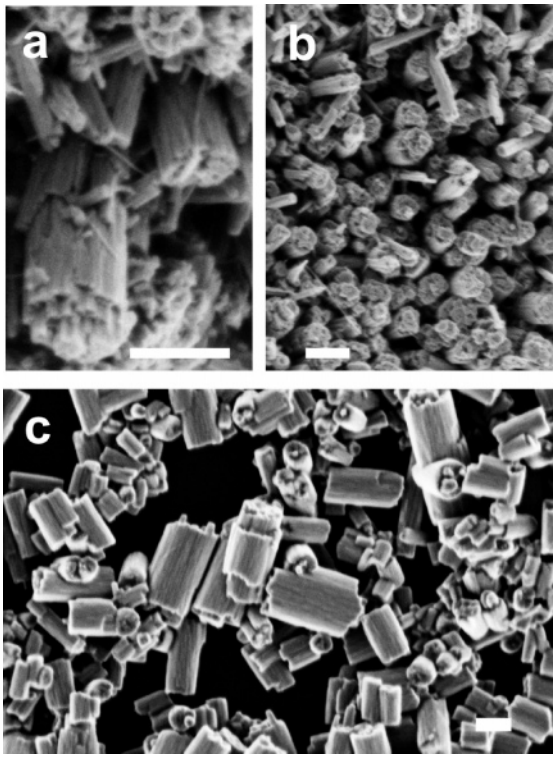

Figure 5. Representative SEM images (scale bar = 200 nm) of nanostructured Rb−HTB tungstate rods synthesized under standard conditions (a, b) and Rb−HTB nanoparticles grown from diluted RbCl/AMT/H_2O solutions (c(W) = 0.007 M in H_2O) (c).

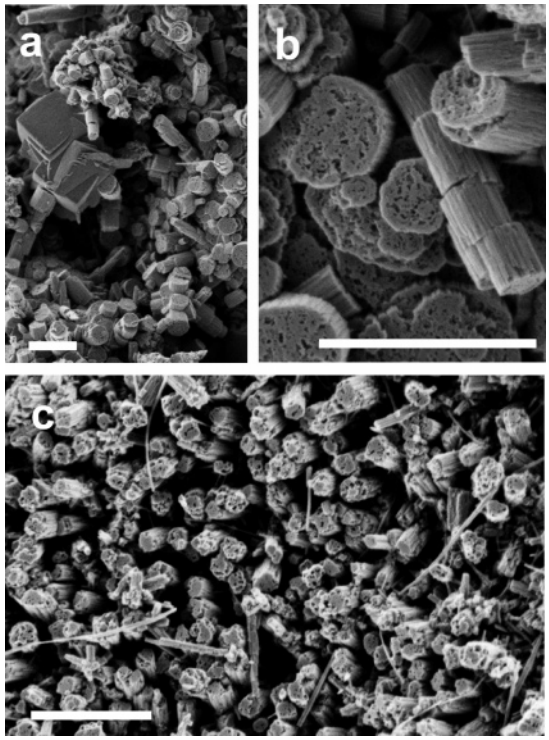

Figure 6. Representative SEM images (scale bar = 800 nm) of nanostructured Cs−HTB tungstate rods synthesized under standard conditions (a, b) and Rb−HTB nanoparticles grown from diluted RbCl/AMT/H_2O solutions (c(W) = 0.007 M in H_2O) (c).

3.1.2.5. CsCl/AMT Systems. The morphology of Cs−HTB tungstates is similar to their Rb analogues except for a strong tendency of the individual hierarchically structured cylinders (Figure 6) toward arrangement into microspheres on the next level (Figure S4c).

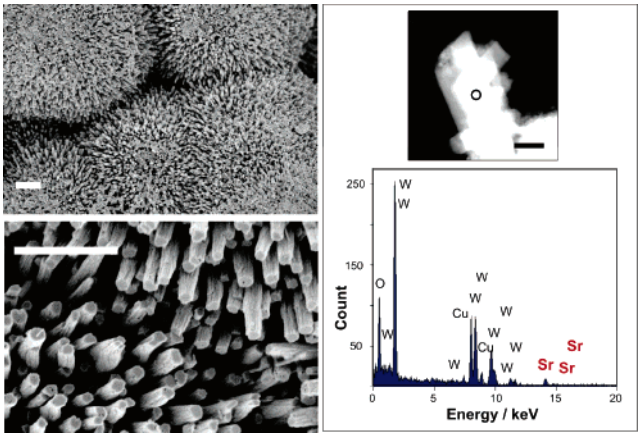

Figure 7. Representative SEM images (scale bar = 1 μm; left) and EDX spot analysis (scale bar = 100 nm) of nanostructured Sr−HTB tungstates.

Under standard hydrothermal conditions they are formed together with pyrochlore cesium tungstates. The latter exhibit a characteristic microscale cubic morphology (Figure 6a). To date, few synthetic approaches toward phase-pure Cs−HTB tungstates are known (cf. Table S1).[15] In this study, we present a new hydrothermal pathway to phase-pure nanostructured hexagonal cesium tungstates. They can be obtained from the CsCl/AMT/HAc system with initial tungsten concentrations around 0.007 M (Figure 6c).

Formation of phase-pure Cs−HTB from low AMT concentrations agrees well with previous studies on the reaction of ammonium paratungstate (ATP: $(NH_4)_{10}W_{12}O_{41}\cdot 5H_2O$) under reflux conditions in acetic acid/ethylene glycol/ethanol media.[17a] Formation of HTB and P phases depends on the solubility of the ATP precursor: when the precursor material is dissolved completely before the reaction is started, the HTB−ammonium tungstate is formed, whereas an immediate reaction without previous dissolution of ATP leads to formation of the P−ammonium tungstate. Consequently, partial dissolution of ATP leads to a mixture of both phases.[17a]

3.1.3. Alkaline Earth Cations. Although a new 2D pyrochlore type has been proposed for Tl, Ba, and Pb tungstates,[12] screening experiments in the $BaCl_2$/AMT/HAc system only afforded a Ba−HTB phase with no distinct morphological features. Previous experiments in the presence of Sr^{2+} failed to afford Sr-based tungstates.[12] Nevertheless, hydrothermal reactions with low tungstate concentrations (c(W) = 0.07 M) in the $SrCl_2$/AMT/HAc system have now brought forward the first Sr−HTB tungstate (Figure 7). The new compound forms microspheres with diameters of 3−6 μm that are hierarchically substructured into rods with an average diameter of 100 nm (Figure 7, left, bottom). The presence of strontium in the individual rods has been verified in terms of EDS spot analyses (Figure 7, right). Elemental analyses indicate the presence of ammonium cations in addition to Sr^{2+}.

3.2. Microwave-Hydrothermal Experiments. In order to investigate the influence of microwave-hydrothermal conditions on the phase and morphology of the emerging

(36) Gerand, B.; Nowogrocki, G.; Figlarz, M. *J. Solid State Chem.* **1981**, *38*, 312.

Table 3. Microwave-Hydrothermal Synthesis of Alkali Tungstates for Comparison with Conventional-Hydrothermal Reactions

cation	(M:W)	phase	morphology
AMT only	reference	O	microflowers (av. 6 μm) made of sheets (<100 nm thick)
LiCl	1:2	HTB	nanorods, *d* ca. 40 nm, *l* ca. 500 nm
LiCl	5:1	O	microflowers (max. 6 μm) made of sheets (50 nm thick)
RbCl	1:2	HTB	microspheres (2−4 μm) made of rods (ca. 200 × 30 nm)
RbCl	5:1	HTB	agglomerated nanorods (ca. 100 × 50 nm)
CsCl	1:2	unknown	microrystals; microspheres (2−4 μm) of rods (*d* 50 nm)
CsCl	5:1	HTB	microspheres (1−3 μm) made of rods (*d* 15−50 nm)

tungstates, we conducted experiments in the AMT/HAc reference system and in the MCl/AMT/HAc (M = Li, Rb−Cs) systems at low and high M:W ratios (1:2 and 5:1). The emerging phases and their morphological features are summarized in Table 3.

3.2.1. AMT/HAc Reference System. Whereas the conventional-hydrothermal synthesis led to formation of HTB-$(NH_4)_{0.26}W_{0.96}O_3 \cdot nH_2O$ nanorods from AMT (Figure 8a, Table 1), microwave-hydrothermal treatments afforded an orthorhombic tungstate, O-$(NH_4)_{0.03}W_{0.99}O_3 \cdot 0.47\ H_2O$ (Figure 8 b), with an XRD pattern that is closely related to orthorhombic $WO_3 \cdot 0.33H_2O$.[36] O-$(NH_4)_{0.03}W_{0.99}O_3 \cdot 0.47\ H_2O$ was formed quantitatively as characteristic microflower-like aggregates (diameters around 4 μm) consisting of hierarchically arranged nanosheets with a thickness of 100 nm and below.

Previous conventional hydrothermal syntheses of $WO_3 \cdot 0.33H_2O$ demonstrated that a rather narrow temperature window (<120 °C) must be maintained for its formation.[34]

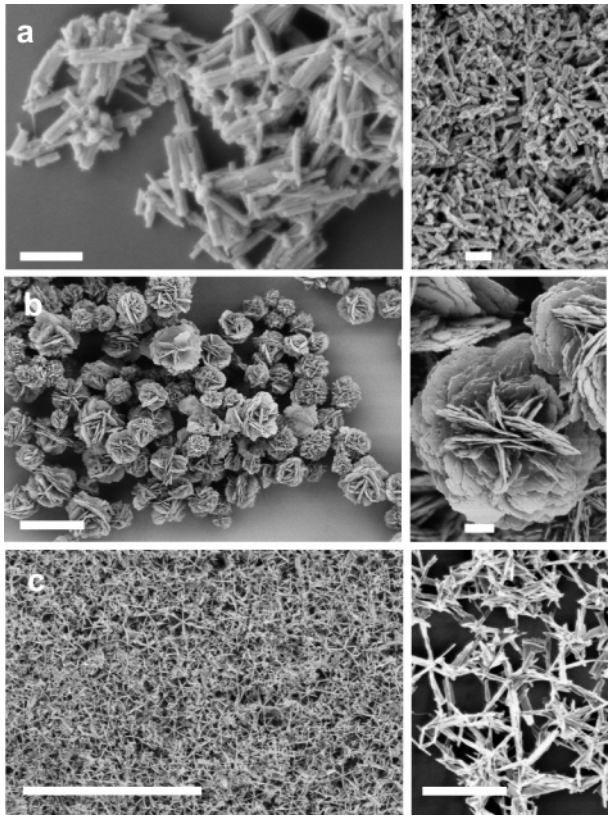

Figure 8. Representative SEM images of (a) NH_4–HTB nanorods formed under standard hydrothermal conditions in the AMT/HAc system (scale bar = 200 nm), (b) orthorhombic ammonium tungstates(VI) synthesized from microwave-hydrothermal synthesis (AMT/HAc; scale bar = 10 μm (left) and 1 μm (right)), and (c) lithium tungstates synthesized from microwave-hydrothermal treatment with a M:W ratio of 5:1 (scale bar = 1 μm).

Furthermore, previous work has shown that the emerging morphology is very sensitive toward the preparative conditions: hydrothermal reaction of pretreated tungstic acid gel under N_2/O_2 atmosphere yielded micrometer-sized needle aggregates of $WO_3 \cdot 0.33H_2O$, while hydrothermal treatment of ripened $WO_3 \cdot 2H_2O$ provided microscale octagonal platelets of $WO_3 \cdot 0.33H_2O$.[36] Therefore, the microwave-hydrothermal approach is a novel and efficient pathway to obtain nanostructured orthorhombic tungstates in gram quantities.

3.2.2. LiCl/AMT Systems. Microwave-hydrothermal treatment at low LiW ratios affected neither the phase nor the morphology of the emerging Li−HTB tungstates (Figure 8c) with respect to conventional-hydrothermal reference experiments (Figure 3a). The lithium content of the products has been determined as $(NH_4)_{0.02}Li_{0.10}W_{0.98}O_3 \cdot 0.64\ H_2O$, and it is in the range of the Li:W ratios obtained from conventional-hydrothermal experiments. When a M:W ratio of 5:1 was applied, however, the orthorhombic phase was formed. It exhibits the same hierarchically structured microflower morphology that has been observed in the AMT/HAc system (Figure 8b), whereas a conventional-hydrothermal reference experiment in the presence of excess LiCl at the given tungsten concentration afforded Li−HTB nanorods. The morphology of the orthorhombic lithium tungstates grown under microwave-hydrothermal conditions differs considerably from the particle shape of orthorhombic lithium tungstates obtained under conventional-hydrothermal conditions (Figure 3b,c). Despite the high Li:W ratio in the starting material, the lithium content of the flower-like orthorhombic tungstate was determined as $(NH_4)_{0.10}Li_{0.02}W_{0.98}O_3 \cdot 0.66\ H_2O$, thereby pointing to a very limited lithium uptake of the orthorhombic phase.

3.2.3. CsCl/AMT Systems. While the RbCl/AMT/HAc systems showed little response toward microwave-hydrothermal treatments, they drastically altered the course of the reaction in the CsCl/AMT/HAc system at low Cs:W ratios (Table 3, Figure 9b). Instead of the expected Cs−HTB or Cs−P tungstates, microcrystals of a cesium tungstate with an approximate Cs:W ratio of 1:5.6 were obtained. The XRD pattern of the product resembles $Cs_4SiW_{12}O_{40} \cdot 13H_2O$ and $Cs_6ZnW_{12}O_{40} \cdot 8H_2O$,[37] but no significant amounts of heteroatoms could be found in the product. The crystal structure is probably cubic with a ~11.85 Å (*Pn*-3*m*), and further investigations are in progress. Hierarchically structured cesium tungstate microspheres are formed as a side product, and their fraction is close to the detection limit of the XRD method. However, Cs−HTB tungstate with a similar sub-

(37) (a) $Cs_4SiW_{12}O_{40} \cdot 13H_2O$: Varfolomeev, M.; Lunk, H.; Feist, M.; Hilmer, W. *Russ. J. Inorg. Chem.* **1989**, *34*, 361. (b) $Cs_6ZnW_{12}O_{40} \cdot 8H_2O$: JCPDS-No. 43-0001.

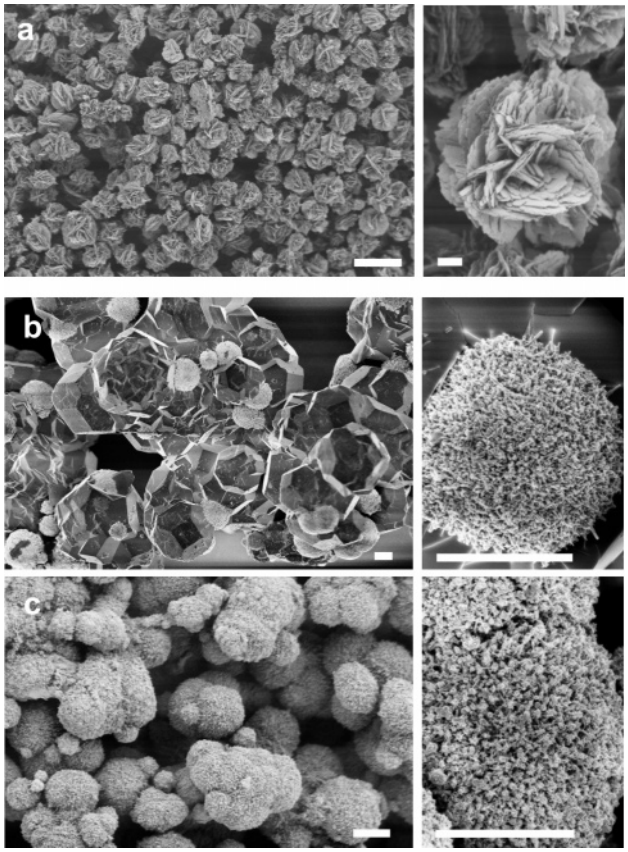

Figure 9. Representative SEM images (scale bar = 1 μm) of lithium tungstates synthesized from microwave-hydrothermal treatment under standard conditions (a) and cesium tungstates synthesized from microwave-hydrothermal treatment under standard conditions (b) and starting from a M:W ratio of 5:1 (c).

structured spherical morphology was obtained from microwave-hydrothermal treatments in the presence of excess CsCl (Figure 9c, Table 3). Therefore, microwave-hydrothermal syntheses are an elegant option to shorten the optimization work that is required to set up a soft chemistry route to nanostructured, phase-pure Cs−HTB tungstate.[15]

In summary, microwave-hydrothermal techniques are a straightforward and effective method to expand the product spectrum of nanostructured alkali/ammonium tungstates.

3.3. Conventional-Hydrothermal Synthesis: Influence of the Reaction Time. In order to gain a deeper understanding of the role of the reaction time and course of the reaction, selected MCl/AMT systems were subjected to variation of the reaction time ranging from 1 h to 18 days (standard reaction time = 2 days, cf. Experimental Procedures). The resulting phases and morphologies are summarized and compared to reference experiments (standard conditions, 2 days) in Table 4.

3.3.1. Short- and Long-Time Experiments. Quantitative conversion of AMT into M−HTB tungstates in the presence of the smaller cations (M = Li− Na) is finished after 2−4 h of hydrothermal treatment. However, the morphology of the products still exhibits a considerable degree of agglomeration (Table 4) so that longer reaction times are required to obtain separate rod-shaped particles.

Generally, the typical morphology of the nanostructured alkali tungstates remains unchanged after 18 days of hydrothermal treatment (Table 4). No particle ripening or further agglomeration is observed for orthorhombic lithium tungstates and Cs−HTB tungstates (cf. Figure S4). Prolonged reaction times enhance the crystallinity of most products. As a result, the potassium tungstate fibers are no longer amorphous (cf. above), but they display two sharp prominent reflections around $2\theta = 23°$ and 47°. These are typical (00l) or (*h*00) reflections for several tungsten oxide hydrates, so that the structure of the potassium tungstate nanorods emerging after 18 days of hydrothermal treatment may contain a layered motif. Note that a hypothetical lamellar compound represented as $K^+[K_5W_{18}O_{57}]^-$ would be formed if every seventh layer of a $K_{1/3}WO_{3+1/6}$ tungstate were vacant and potassium cations were inserted instead.[16]

3.4. Time-Dependent Conversion of AMT into Nanostructured Tungstates: In Situ EXAFS and Ex Situ Quenching Experiments. Next, the time scale of tungstate formation was estimated more precisely with the help of ex situ quenching experiments performed in the AMT/HAc and CsCl/AMT/HAc systems. In addition, time-dependent formation of nanostructured tungstates was studied with in situ EXAFS experiments performed in an EXAFS cell that is similar to an autoclave with PEEK inlay (cf. Experimental Procedures and references therein).[38] Due to the similar local environment of tungsten both in the AMT precursor and in the HTB tungstates, EXAFS spectra were required to uncover the structural transformations. All products emerging from in situ EXAFS experiments were subsequently characterized in terms of XRD patterns and SEM images (cf. Figures 10 and 12).

3.4.1. Time Scale of Hexagonal Formation in the AMT/HAc System. The ex situ experiments in the AMT/HAc system starting from low tungsten concentrations (0.05 M) reveal that conversion of AMT into the rod-shaped hexagonal tungstate phase is in progress between 1 and 2 h of reaction time (Figure 10). After 1 h, the surface of the starting material exhibits the first onset of nanostructuring (Figure 10a (top)), but the small amount of material formed was not sufficient for XRD analysis. Formation of nanorods sets in around 2 h (Figure 10b (top)), and the XRD pattern indicates that AMT has been converted into the hexagonal tungstate phase in the presence of amorphous residual material. Prolonged hydrothermal treatments (2 days) are required to finalize the growth process of the nanorods and improve the crystallinity of the final product (Figure 10d).

In situ EXAFS investigation of the AMT/HAc system with a tungsten concentration of 0.05 M in the starting material revealed that during stepwise heating to 200 °C, no changes at all—neither in the XANES nor in the EXAFS region—were detected, indicating that the symmetry around the W absorber atom did not change and no solid materials were formed. At 200 °C, only after more than 2 h a change in both the XANES and the EXAFS spectrum was observed, indicating the onset of the reaction (Figure 11).

After 4 h, phase-pure HTB tungstate nanorods were formed (Figure 10c). These observations agree well with the ex situ experiments but may be slowed down due to the lower

(38) (a) Ramin, M.; Grunwaldt, J.-D.; Baiker, A. *J. Catal.* **2005**, *234*, 256. (b) Rohr, M.; Grunwaldt, J.-D.; Baiker, A. *J. Catal.* **2005**, *229*, 149.

Table 4. Hydrothermal Parameters and Emerging Phases and Morphologies of Short-Time and Long-Time Experiments in the MCl/AMT Systems (M = Li−Cs)[a]

MCl/parameter	*c*(W)	*t*/h	phase	morphology change compared to 2 days	
			short-time experiments		
LiCl/220 °C	0.07	2	HTB	nanorods, *d* 20−30 nm, *l* 200−400 nm	NO
NaCl	0.07	4	HTB	microspheres consisting of rods (*l* ca. 1 μm, *d* ca. 100 nm)	−
NaCl/220 °C	0.07	2	HTB	rods: length ca. 2 μm, *d* 100−200 nm, intergrown	−
			long-time experiments		
LiCl	0.07	18	HTB	nanorods, *d* 20-30 nm, *l* 200−400 nm	NO
LiCl	0.007	18	O	microflowers with dendritic nanorods	NO
NaCl	0.07	18	HTB	rods: *l* ca. 3 μm, *d* ca. 100 nm	NO
NaCl/H_2O	0.007	18	HTB + amorph.	rods: *l* ca. 12 μm, *d* ca. 100 nm + microplatelets (side product)	NO
KCl/H_2O	0.007	18	Layered cpd.	rods: *l* up to 2 μm, *d* < 100 nm	NO
RbCl/H_2O	0.07	18	P, little HTB	HTB: few hierarchical rods, ca. 100 × 200 nm	NO
CsCl	0.007	18	HTB	hierarchical microspheres made of stacked rods (ca. 200 × 800 nm)	+
CsCl/(Cs:W) = 4	0.5	18	HTB + P	HTB: stacked rods (ca. 200 ×800 nm), slightly improved	+

[a] + = Morphology improved with respect to 2 day reaction time. − = Morphology deterioration with respect to 2 day reaction time. NO = no significant change.

concentration of AMT in the solution. Note the significant difference to the previously reported XANES/EXAFS data on formation of MoO_3 nanorods: in this hydrothermal system the structural changes occurred more rapidly.[26] Since the local environment of tungsten changes only slightly, more detailed EXAFS spectra were required here and XANES data were not sufficient as, for example, in the hydrothermal synthesis of MoO_3 from $MoO_3 \cdot 2H_2O$.[26]

3.4.2. Reaction Time scale in the CsCl/AMT/HAc System. The ex situ kinetic experiments in the CsCl/AMT/HAc system demonstrate that the reaction time scale is not significantly altered when the tungsten concentration in the system is kept at 0.05 M and CsCl is added (1 M). Like in the AMT/HAc system, very little product exhibiting surface nanostructuring precipitates after 1 h (Figure 12a, top), and

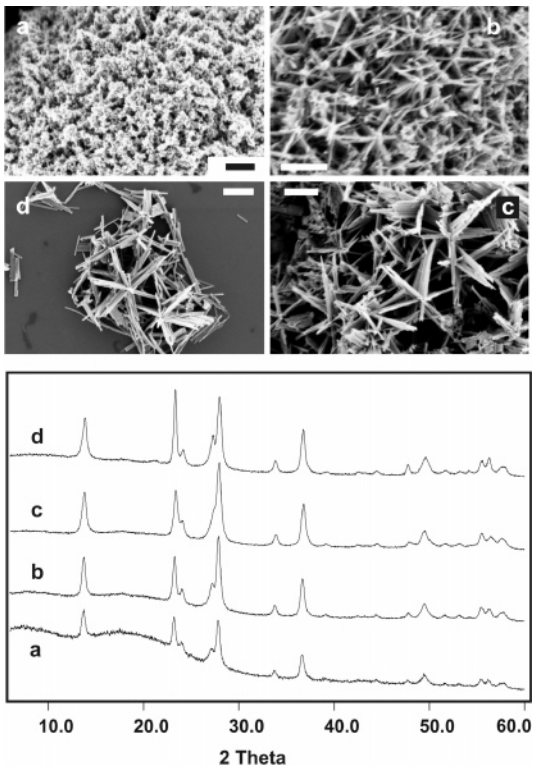

Figure 10. SEM images (top; scale bar = 400 nm) and XRD patterns (bottom) monitoring the time scale of NH_4–HTB tungstate formation; (top) (a) 1 h (ex situ), (b) 2 h (ex situ), (c) 4 h (in situ EXAFS), (d) 2 days (standard hydrothermal conditions), (bottom) (a) 2 h (ex situ), (b) 3 h (ex situ), (c) 4 h (in situ EXAFS), (d) 2 days (standard hydrothermal conditions).

the XRD pattern recorded after 2 h of reaction time indicates the presence of phase-pure Cs−HTB tungstate and amorphous residues.

After 2 days of reaction time, the starting material has been quantitatively converted into hierarchically structured microspheres (Figure 12c). As outlined above, their crystallinity and morphology is further improved by 18 day-treatments (Figure 12d).

Addition of CsCl had no effect on the respective in situ EXAFS experiments as well: at 200 °C, no products were observed before an induction time of 2 h, so that the AMT/HAc and the CsCl/AMT/HAc systems display similar kinetics. Figure 12b shows that phase-pure Cs−HTB tungstate has been formed after a reaction time of 4 h in the in situ EXAFS cell (bottom) and that the characteristic stacked nanorods are beginning to emerge (top). In both systems investigated, only small changes occur during cooling from 200 °C to room temperature. Their reaction kinetics proceed on an hour scale and differ considerably from the previously studied hydrothermal synthesis of MoO_3 nanorods.[26,31]

3.5. Time-Dependent Conversion of AMT into Nanostructured Tungstates: In Situ EDXRD Investigations. Ex situ experiments conducted at higher tungsten concentrations (0.67 M) in the AMT/HAc system indicated that conversion of the starting material into nanoscale tungstates begins after approximately 19 min. This observation points to a quicker onset than has been observed for lower tungsten contents in the starting material (cf. section 3.4). Generally, product formation under solvothermal conditions depends on several experimental parameters, e.g., pH value, temperature, volume, pressure, and/or kind of educt source.[33,34,37] In the previous section, it was clearly demonstrated that the presence of the alkali cation significantly influences the morphology of the reaction product. Therefore, the influence of these ions onto the kinetics and the mechanisms of crystal growth were studied with in situ EDXRD experiments starting from tungsten concentrations of 0.67 M at a reaction temperature of 200 °C. In the energy range chosen several reflections of the product and W resonances were monitored simultaneously (Figure 13).

A typical sequence of time-resolved spectra is shown in Figure 13. After an induction time t_{ind} that depends on the kind of alkali ion, the product peaks of the hexagonal

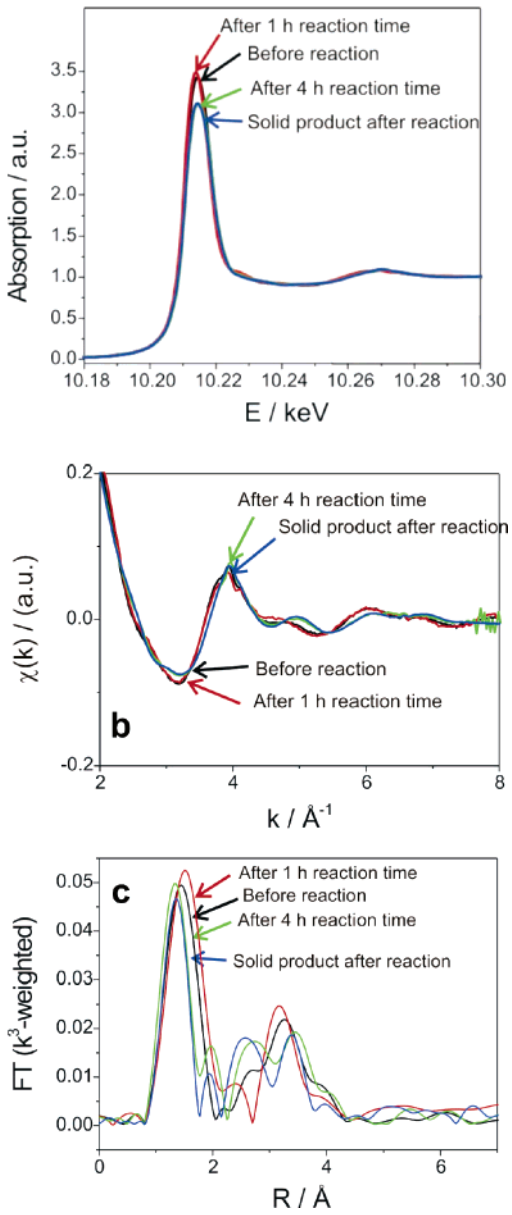

Figure 11. (a) XANES and (b) EXAFS data at the W L_3-edge taken during hydrothermal synthesis of nanostructured ammonium tungstate from AMT; (c) corresponding Fourier-transformed EXAFS data (k^3-weighted $\chi(k)$ function).

tungstate phase started to grow. Note that the peaks at 57.98 and 59.31 keV are due to the W K_α and K_β resonances. The product peak with the highest intensity is the (200) reflection. A quantitative analysis of the growth rates shows identical behavior for different reflections and confirms an isotropic crystallite growth. Deviations of the growth rate due to crystallinity, peak shape, etc., were negligible after internal normalization of the data. No hints are seen in the spectra for the occurrence of crystalline precursors or intermediates.

The integrated intensities of the product reflections were normalized against the intensity of the most intense W K_α resonance. Plots of the extent of reaction α (ratio of the normalized intensity at the reaction time t by the intensity at the time $t\infty$) against the reaction time t (Figure 14) demonstrate that t_{ind} and $t_{0.5}$ depend on the kind of the alkali ion. In general, the presence of alkali ions leads to a decrease of the reaction time, i.e., the chemical reaction is faster with M^+ ions. Interestingly, in the presence of Na^+ and K^+ ions

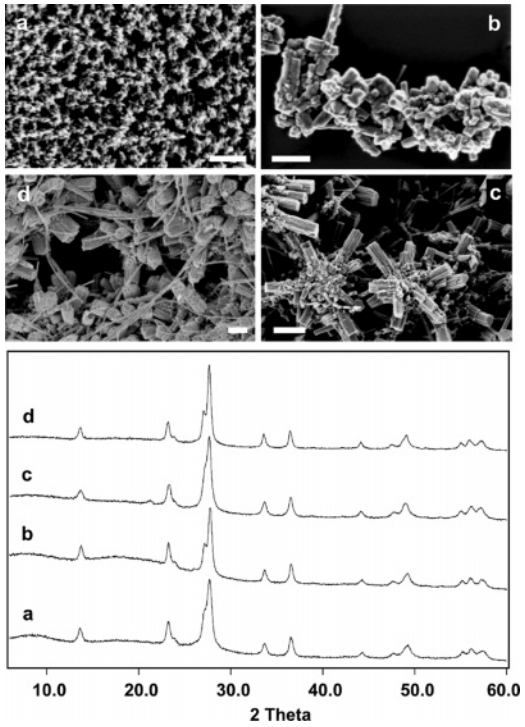

Figure 12. SEM images (top; scale bar = 300 nm) and XRD patterns (bottom) monitoring the time scale of Cs−HTB tungstate formation; (top) (a) 1 h (ex situ), (b) 4 h (in situ EXAFS), (c) 2 days (standard hydrothermal reaction), (d) 18 days (long-time experiment); (bottom) (a) 2 h (ex situ), (b) 4 h (in situ EXAFS), (c) 2 days (standard hydrothermal reaction), (d) 18 days (long-time experiment).

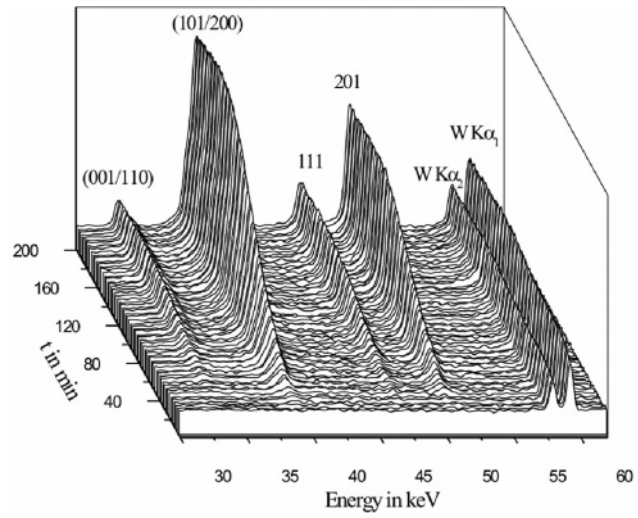

Figure 13. Time-resolved energy-dispersive X-ray powder pattern recorded at 200 °C in the presence of Rb. The indices of the most intense lines of the product phase and W K_α and K_β fluorescence lines are marked.

the induction time is increased while the overall reaction time is shorter than without these ions. In contrast, the presence of Li^+, Rb^+, or Cs^+ reduces both t_{ind} and the half-life time significantly (Table 5).

The morphology of the products formed in the course of in situ EDXRD experiments was investigated in terms of SEM images recorded after the reaction. As observed for the ex situ experiments mentioned above and for the in situ EXAFS studies (cf. Figures 10 and 12), all products show the onset of nanostructuring, but longer reaction times are required to fully develop the characteristic particle morphologies depending on the cation (Figures 3−5).

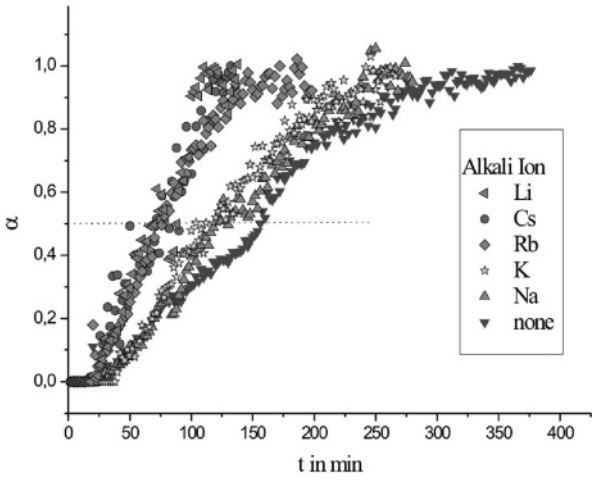

Figure 14. Extent of reaction α versus time for the (101/200) reflections for different alkali ions.

Table 5. Kinetic Data for All in Situ EDXRD Experiments

cation	t_{ind}/min	$t_{0.5}$/min	reaction time/min	*m*	growth model
none	14	134	292	1.4	A2/A3
Cs	9	71	143	1.6	A2/A3
Na	21	103	225	1.4	A2
Rb	11	67	151	1.6	A2
K	33	77	223	1.3	A2/R3
Li	12	68	130	1.5	A2

3.5.1. Kinetic Analysis. Kinetic studies are useful because quantitative information such as half-life and rate constants can be evaluated. In addition, information about the reaction mechanism is acquired. Kinetic analyses are performed by fitting the experimental data to a theoretical expression relating the extent of reaction α vs time. Several kinetic expressions applied to solid-state kinetics have been reported, and the general shape of their curves is well documented. A detailed description of evaluation of data has been provided in the literature.[33] The kinetic evaluation was performed after subtracting the induction time t_0 from time *t*. The kinetic data for different reactions are summarized in Table 5. When $\ln[-\ln(1-\alpha)]$ versus $\ln(t)$ is plotted (the so-called Sharp−Hancock plot, abbreviated SH), a straight line is obtained for that part of the reaction which follows the same mechanism.[40] A change in the mechanism during the reaction leads to a change in the slope of the curve. From the slope of the linear part of the curve the reaction exponent *m* can be evaluated. The Avrami exponent *m* is related to the type of nucleation and growth process taking place, including the morphology of the reaction product, i.e., whether the crystals are fibers, needles, plates, sheets, spheres, or polygons. The exponent *m* also includes the type of nucleation, i.e., whether the nuclei all develop at once or there is a continuous nucleation with a constant rate.[41,42] While the induction times and half-life times depend on the presence of the alkali ion, no influence onto the reaction mechanism is observed. A typical SH plot is shown in Figure 15a.

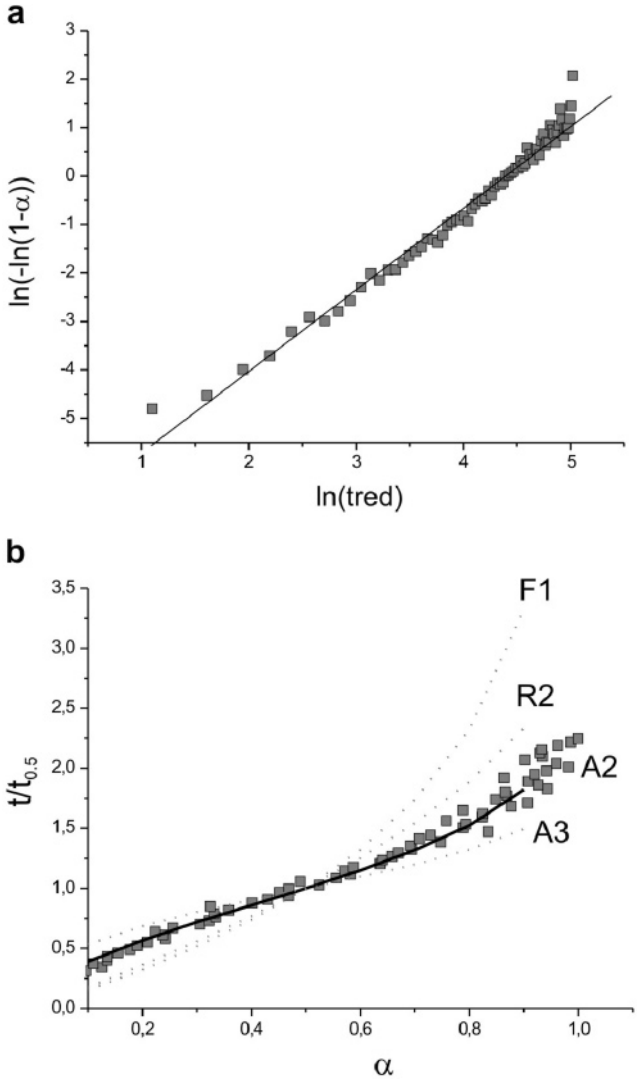

Figure 15. (a) Sharp−Hancock plot and (b) comparison of the evolution of experimental $t/t_{0.5}$ data as a function of α (gray squares) with different theoretical models. The letters with the numbers are abbreviations of the different models listed in Table S2.

The experimental points are on a straight line over the whole reaction indicating that there is no change of the reaction mechanism. The reaction exponent *m* has a value of ∼1.5 (Table 5) which is in the region of values for phase boundary control and nucleation-controlled growth mechanism (Table S2, mechanism A2, $m = 2$).

For more detailed and rigorous analyses different models (collected in Table S2) were compared with the experimental data.[43] In order to select the most appropriate model, the experimental $t/t_{0.5}$ data ($t/t_{0.5}$ is the reaction time at $\alpha = 0.5$) are plotted vs α. The result is shown in Figure 15b, and the procedure allows a direct comparison with the different models under consideration. For all reactions the experimental data fit with nucleation control (model A2, Table S2), confirming the results from the SH plots discussed above.

(39) (a) Kiebach, R.; Schäfer, M.; Porsch, F.; Bensch, W. *Z. Anorg. Allg. Chem.* **2005**, *631*, 369. (b) Francis, R. J.; Price, J. S.; Evans, J. S. O.; O'Brien, S.; O'Hare, D. *Chem. Mater.* **1996**, *8*, 2102. (c) Bray, H. J.; Redfern, S. A. T. *Phys. Chem. Miner.* **1999**, 591.(d) Christensen, A. N.; Bareges, A.; Nielsen, R. N.; Hazell, R. G.; Norby, P.; Hanson, J. C. *J. Chem. Soc., Dalton Trans.* **2001**, 1611.

(40) (a) Hancock, J. D.; Sharp, J. H. *J. Am. Ceram. Soc.* **1972**, *55*, 74. (b) Sharp, J. H.; Brindley, G. W.; Narahari Achar, B. N. *J. Am. Ceram. Soc.* **1966**, 379. (c) Mohamed, B. M.; Sharp, J. H. *J. Mater. Sci.* **1997**, 1595.

(41) Brown, P. W.; Pommersheim, J.; Frohnsdorff, G. *Cem. Concr. Res.* **1985**, *15*, 35.

(42) Thomas, J. J.; Jennings, H. M. *Chem. Mater.* **1999**, *11*, 1907.

(43) (a) Avrami, M. *J. Chem. Phys.* **1939**, *7*, 1103. (b) Avrami, M. *J. Chem. Phys.* **1940**, *8*, 212. (c) Avrami, M. *J. Chem. Phys.* **1941**, *9*, 177.

Parallel to their common formation mechanism, all products exhibit in principle a similar anisotropic dimensionality in the initial phase of the reaction. This is in line with the parametrical scope of the reaction exponent *m*. A more detailed interpretation of the individual aspect ratios in relation to *m* would require a series of carefully designed quenching experiments that would go beyond the scope of this study.

However, is has to be pointed out that the morphology (1-dimensional needle-like, sometimes an intermediate between needles and plates) observed for the products of the in situ experiments is clearly in accordance with the value of ~1.5 found for *m* and can be explained by the equation $m = (P/S) + Q$. *P* is the dimensionality (in this case a value between 1 and 2), and the constant *S* is related to the rate-limiting growth mechanism (here a value of 1 for boundary controlled growth is taken). *Q* is a constant which is determined by the nucleation rate (here a value of 0 for nucleation site saturation is reasonable), leading to values for $m \approx 1.5$. For more details concerning the different parameters and use of the equation, cf. ref 39.

4. Discussion

The structure and morphology of nanostructured tungstates generated from hydrothermal field studies[44] depends on the synthetic conditions and cations incorporated into the parent tungstate framework. In the MCl/AMT (ammonium metatungstate; M = Li−Cs) hydrothermal systems, the Li-, Na-, and K-based compounds adopt the hexagonal tungsten bronze (HTB) structure, whereas the presence of Rb^+ and Cs^+ gives rise to both HTB and pyrochlore tungstates. The phase preferences[11] of the individual cations are accompanied by specific morphological profiles: the HTB phases containing lithium, sodium, or potassium exhibit an anisotropic, rod-shaped morphology. Among them, the hexagonal sodium tungstates display maximum values of the aspect ratio. Contrary to the fibrous materials obtained with smaller alkali cations, the rubidium- and cesium-based HTB particles exhibit a hierarchical growth pattern of small nanorods that are stacked into cylindrical arrangements.

The preparative options provided by the alkali chloride additives can be applied upon quick and efficient microwave-hydrothermal production of nanostructured alkali tungstates. For example, optimization work that is usually required to generate phase pure nanoscale Cs−HTB tungstates can be cut out. This method furthermore provides access to flower-like nanostructured orthorhombic tungstates when applied in the absence of alkali cations. Interestingly, the orthorhombic phase can be formed as well with an excess of LiCl in the reaction medium, while lower Li:W ratios lead to microwave-hydrothermal formation of Li-containing HTB nanorods. However, the orthorhombic tungstates take up only negligible amounts of lithium cations, so that their formation might be due to a surface effect of Li^+, thereby rendering it an "additive" in the true sense of the word.

Ex situ and long-time experiments in the MCl/AMT (M = Li−Cs) hydrothermal systems unraveled that the kinetics of nanostructured tungstate growth is generally slower than that observed for hydrothermal formation of MoO_3 fibers.[26] This was verified by a combined in situ EXAFS/EDXRD study: first, conversion of ammonium tungstate into ammonium- and cesium-containing HTB nanorods, respectively, was studied for low AMT concentrations. Under the given conditions, the onset of product formation was observed after approximately 2 h. Furthermore, additional ex situ experiments indicated that the kinetics of HTB nanorod formation might be concentration dependent. As in situ EDXRD methods are better suited for the study of tungstate growth at higher tungsten concentrations, they were subsequently employed to investigate the influence of the alkali cations on the kinetics of the reaction. For a complete monitoring of the structural changes occurring during the transformation of the AMT precursor into hexagonal tungstates, both in situ EDXRD and EXAFS methods are required. Whereas the induction times (10−30 min) vary with the alkali cation, all of them accelerate conversion of AMT into nanostructured tungstates. Nevertheless, the alkali-based hydrothermal processes still take more than an hour to completion, and at least 2 days of further treatment are required to obtain a fully developed anisotropic morphology. Note that the tendency toward nanofiber formation is most pronounced with Na^+ and K^+ that exhibit the longest induction times. In spite of their different induction times, the alkali cations generally support a nucleation-controlled growth mechanism. This general result is in line with the observed morphologies, and the individual reaction profiles of the alkali cations are the subject of a detailed follow-up study. Nucleation control might account for the longer onset times observed for lower AMT concentrations in the in situ EXAFS experiments: all in all, both in situ approaches demonstrate that the hour-scale kinetics of ammonium tungstate formation is slow in comparison with the hydrothermal preparation of MoO_3 rods that is quantitatively finished after a maximum of 15 min.[26] However, the morphology of the MoO_3 rods cannot be controlled with the help of alkali cations to a comparable extent.[45]

5. Conclusion

The present study outlines how the one-step hydrothermal formation of nanostructured tungstates can be altered by alkali halides to generate alkali HTB tungstates with various morphologies. A systematic hydrothermal field study has been conducted to track down the optimal parameter windows for the different product types. Their formation process has been explored with a combination of in situ EXAFS and EDXRD methods, so that key mechanistic and kinetic information is now available to fine tune the synthetic protocol for further applications. The presence of alkali cations speeds up the hydrothermal process. Although they all support a nucleation control mechanism for formation of nanostructured hexagonal tungstates, their individual reaction kinetics differ from each other. Further studies are now

(44) Behrens, P.; Glaue, A.; Haggenmüller, C; Schechner G. *Solid State Ionics* **1997**, *101*, 255.

(45) Michailovski, A.; Krumeich, F.; Patzke, G. R. *Helv. Chim. Acta* **2004**, *87*, 1029.

required to investigate whether the kinetic behavior of the alkali cations is linked to their different morphological profiles in the hydrothermal synthesis of nanostructured tungstates. In this way, combination of hydrothermal parameter screenings with complementary in situ techniques is a step toward the true "design" of tungsten oxide-based nanomaterials.

Acknowledgment. We thank Prof. Dr. R. Nesper (Laboratory of Inorganic Chemistry, ETH Zürich) for his steady interest and continuous support of this work. We gratefully acknowledge ANKA (Karlsruhe, Germany) for providing beamtime at beamline ANKA-XAS for in situ EXAFS experiments and HASYLAB (DESY, Hamburg, Germany) for providing beamtime at beamline F3 for in situ EDXRD experiments. We are grateful to Prof. Dr. Detlef Günther and Ms. Kathrin Hametner (Laboratory of Inorganic Chemistry, ETH Zürich) for LA-ICP-MS analyses. We thank Dr. Feng Gao (Pennsylvania State University) for carrying out microwave syntheses and Dr. Denis Sheptyakov (Paul Scherrer Institute, Villigen, Switzerland) for structural investigations of cesium tungstates. This work was supported by the ETH Zürich, Swiss National Science Foundation (MaNEP−Materials with Novel Electronic Properties), and National Research Program "Supramolecular Functional Materials".

Supporting Information Available: Overviews concerning the synthesis of tungstates and rate equations for solid-state reactions; preparative details of the hydrothermal preparation of alkali HTBs (SEM images). This material is available free of charge via the Internet at http://pubs.acs.org.

CM061020O